Rotor Slot Design of Squirrel Cage Induction Motors with Improved Rated Efficiency and Starting Capability

Mauro Di Nardo, *Member, IEEE,* Alessandro Marfoli, Michele Degano, *Senior Member, IEEE,* Chris Gerada, *Senior Member, IEEE*

***Abstract*—Among the electro-mechanical devices transforming energy from electrical to mechanical, the squirrel cage induction motor can be surely considered a workhorse of the industry due to its robustness, low cost and good performance when directly fed by the a.c. grid. Being the most influencing motor topology in terms of energy consumption, optimizing the efficiency of squirrel cage induction motors could lead to a great impact towards the reduction of the human environmental footprint. The induction motor design aided by finite element analysis presents significant challenges because an accurate performance prediction requires a considerable computational burden. This paper makes use of an innovative fast and accurate performance evaluation method embedded into an automatic design procedure to optimize different rotor slot geometries. After introducing the performance estimation approach, its advantages and limits are discussed comparing its prediction with the experimental tests carried out on an off-the-shelf induction motor. Different rotor cage structures with increasing geometrical complexity are then optimized in terms of starting and rated performance adopting the same design optimization process, the same stator geometry and constituent materials. The analysis of the optimal solutions shows how it is possible to improve the rated efficiency without compromising other performance indexes. The presented results can be used as general design guidelines of squirrel cage induction motors for industrial applications.**

***Index Terms*—Boucherot Bar, Efficiency, Finite Element Analysis, Fast Performance Computation, Induction Motor, Multi-Objective Optimization, Squirrel Cage, Rotor Slot Design.**

I. Introduction

There are several reasons why a really wide variety of cross-sectional shapes for cast-aluminium rotor bars have been used by squirrel cage induction motor (SCIM) manufacturers over the last century. On the one hand, the manufacturing of complex rotor geometries, within reasonable limits, it does not essentially require any additional cost with respect to the simpler structures. On the other hand, by modifying the rotor slot cross section, thus its resistance and leakage inductance, it is possible to satisfy a wide range of requirements in terms of starting, breakdown, pull-up torques, starting current, rated efficiency and power factor. The above considerations have led most of the induction motor manufacturers to explore various rotor slot shapes (sometimes referred with fancy names such as flowerpot, doghouse, barbells, etc.) to satisfy the performance requirements of SCIMs [1], [2].

M. Di Nardo, A. Marfoli, M. Degano and C. Gerada are with the Power Electronics and Machine Control Group, University of Nottingham, UK, e-mail: mauro.dinardo4@nottingham.ac.uk

The variety of cross sectional shapes used for fabricated rotor bars, usually adopted for high power ratings, is considerably more limited with respect to the cast-aluminium ones. This is mainly due to both the increased cost of machining complex bars and the increased rotor radial dimensions, which naturally enhances the deep bar effect [3]. The latter is the well-known phenomena for which the current density distribution within a solid conductor placed in a magnetic core is non uniform and tends to be crowded towards the outer part (i.e. the one closer to the main airgap). This is due to the fact that the innermost parts of the conductor see a greater amount of leakage flux (respect to the outermost parts); therefore the corresponding reactance is higher while the current is lower in module and lagging in phase with respect to the currents in the upper parts. This effect has been traditionally exploited to obtain high effective resistances at the starting condition (due to the uneven current distribution) and low resistance at the rated operating point (where the current density is uniform since the reactance at low frequency plays a minor role). The exact analytical solution of the bar resistance and leakage inductance as function of the geometry and frequency can be obtained only for rectangular and trapezoidal cross-sections [4]–[6], while the unsaturated DC leakage inductance can be instead calculated for a wide range of slot shapes [7]. From these formulations it is easy to understand that simple deep bar designs are of limited usefulness when a really high starting torque is needed; in such cases, the bar depth to width ratio becomes unreasonably large and mechanically unfeasible/undesirable [4]. Consequently some of its variants, such as L-shaped, inverse T-slot, inverse trapezoidal-shape, have been usually preferred (especially for fabricated rotor bars) also for their improved structural and thermal behaviour [8], [9]. With the aim of further increasing the starting torque and at the same time lowering the corresponding current, the double cage concept was introduced at the beginning of the last century first by Dolivo-Dobrovolski and later by Boucherot [7]. In this case, the rotor carries two concentric cages made of a set of outer bars having high resistance and low leakage inductance and a set of inner bars with low resistance and high leakage inductance. The upper and inner parts of the slot are connected by a slit, also called leakage slot, which is needed to increase the leakage inductance of the innermost bar and also to avoid that the latter part is missed by the main flux linkage during the normal operation at low rotor frequency [10]. At the starting condition, the higher innermost slot leakage

reactance forces the current to flow in the outermost cage which has been appropriately designed with a higher resistance (i.e. low cross-section and/or material with higher resistivity such as brass, aluminium, etc). This leads to the desired enhancement of starting performance. At the rated operating point, the leakage reactance becomes a negligible part of the rotor impedance and so the current density becomes more uniformly distributed and the effective resistance proportional to the parallel of the single bars resistance. This in turn allows to achieve a relatively high efficiency being the innermost cage suitably designed to have a low DC resistance (high cross-section bar made of good electric conductible material such as copper). When a Boucherot cage is manufactured by die-casting, so for low-medium power range, both upper and lower slots including the connecting slit are filled with the same material. By playing on the geometry of the double cage, it is possible to achieve almost any torque-speed characteristic (within reasonable limits) [4], [11]. Respect to the single cage structure, the Boucherot bar features a higher leakage reactance also at the breakdown operating condition, and this leads to a lower maximum torque. Although the bar resistance and leakage inductance can be calculated via an analytical numerical method (e.g. slicing approach [7], [12]) for any rotor slot geometry, the influence of the iron saturation is more difficult to predict especially in the case of closed rotor slots. The latter are usually preferred to the open variants mainly for mechanical reasons. In fact, a closed rotor slot structure makes easier the die-casting process and it allows an accurate machining of the rotor surface if needed [13], [14]. As a positive side-effect, a smooth rotor surface reduces the flux pulsation due to the rotor slotting, and so in some cases it is possible to appreciate lower surface iron losses and lower joule losses due to the reduced harmonic content of the stator current [14]–[16]. As a negative side-effect, the higher slot leakage inductance causes the reduction of the breakdown and starting torque and rated power factor and efficiency [17]. In case of open rotor slots, an estimation of the saturated leakage inductance can be done using a corrected value of the slot opening obtained iteratively calculating the permeability of the tooth tips [7]. A similar approach can be also applied when adopting closed slot geometries although more refined methods consisting in dividing the iron bridge into parallel strips are presented in [7], [18]. The effects of the non-uniform current density distribution within the rotor bar and the iron saturation are usually separately considered via analytical means neglecting the mutual interaction between these two different phenomena. This approximation could be acceptable for certain slot geometries and operating conditions, and cannot be considered general. For example, in small-medium power SCIMs with deep and narrow closed slots, the bridge permeance could become a relevant portion of the overall leakage permeance; so a modelling error of the former can negatively affect the accuracy of the performance estimation [14]. The same issue is encountered when the iron part between the upper and lower bars of a Boucherot cage saturates; in such case, the effective slit width is higher and the leakage inductance differs from the unsaturated designed value (especially when the radial dimension of such slit is small) [1]. The above-mentioned analytical approaches are useful during the initial stage of the design, which is often followed by a finite element (FE) refinement. Clearly only the latter can provide a rigorous simultaneous treatment of these complex phenomena.

II. Aims and Structure of the Work

The analysis and design of SCIMs is a well-known and consolidated topic. Starting torque and current, pull-up and breakdown torques, rated efficiency and power factor are the performance indexes to consider during the SCIM design. All these performance indexes have to comply with the boundaries defined by the national or international standards. In particular, the international standard IEC 60034-30-1 defines different classes of efficiency, as reported in Fig.1, where it can be seen that the minimum efficiency requirement increases with the power rating. The SCIM design presents significant challenges because of the several performance indexes to be considered and their complex relationship with the machine geometry. The design difficulty escalates when it is carried out with the aid of optimization algorithm because the accurate prediction of the performance requires time-consuming FE analysis. Recently published work [19] have proposed a new systematic methodology to carry out the design optimization of SCIMs. An innovative mixed analytical-FE performance evaluation method based on [20], [21] has been introduced, which is able to obtain a very fast estimation of the torque and efficiency behaviour without compromising the results' accuracy. This new performance estimation approach has been embedded within an automatic design procedure aided by stochastic optimization algorithm having the target of maximizing both starting and rated performance. This work further exploits the methodology presented in [17], [19] to explore the potential benefits of the adding geometrical degrees of freedom to the rotor slot geometry. Although the SCIM performance are affected by the whole machine geometry and its constituent materials, this work focuses on the rotor slot design being one of the most important factor. Indeed, standard single and double cage structures are compared with a proposed non-standard rotor slot geometry keeping both stator design and materials unchanged during the optimization and equal to the benchmark machine. The latter, reported with the marker ★

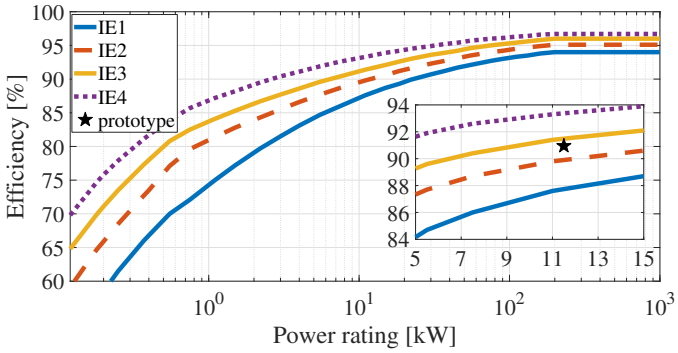

Fig. 1: Efficiency levels defined by IEC 60034-30 for a 4-poles, 50Hz SCIM along with the measured efficiency of the benchmark machine showed in the inset figure.

in Fig. 1, is an off-the-shelf 11.5kW - 4 poles SCIM with a classical double cage structure having an IE2 efficiency class.

The paper has been organized as follows. Section III reports the description of adopted parametrizations. Section IV summarizes the performance estimation methodology while Section V reports the experimental tests carried out on an off-the-shelf SCIM in order to validate the proposed approach. Section VI presents the optimization results of both standard and proposed rotor slot geometries. A deep analysis of the optimal geometries is then discussed in section VII while Section VIII gives the final remarks.

III. Rotor slot parametrizations

Two different closed rotor slot parametrizations are considered in this work. The first one is a generalized Boucherot bar, which allows investigating a wide range of both single and double cage geometries. The second is an enhanced variant of the first one where both upper and lower slot sections are suitably defined by a spline. The latter allows to further widen the slot shapes to explore during the design optimization.

The generalized Boucherot geometry, hereafter called double cage (DC), is described by 7 variables, as shown in Fig. 2a), i.e. the neck width d, the radii of the outer, central and inner circles R_{out}, R_m and R_{in}, the distance between the outer and central circles h_{out} and the central and the inner circles h_m and the external bridge thickness b. All these 7 variables are defined in per unit of their respective maximum values and a detailed description of the drawing procedure can be found in [19]. Fig. 2b) shows some of the bar geometries that can be obtained adopting this per unit parametrization. Clearly most of the standard single and double cage geometries, such as circle, deep bar, trapezoidal-like shape, and all the Boucherot variants can be drawn with this parametrization, which excludes only asymmetric geometries.

Locking some degrees of freedom of this generalized parametrization is possible to explore only single cage structures (hereafter named single cage SC). Indeed, plain rotor slots are obtained considering the distance between the two outer and inner cages null ($h_{out} = 0$) and equal the radii of the outer and middle circles ($R_{out} = R_m$).

Defining the upper and lower profile of a Boucherot bar with a spline instead of more simple arcs of circumference and straight lines, the slot shape variety remarkably increases. Among the many types of splines, the so-called Bézier curve has been selected thanks to its properties which turns to be advantages for this particular case [22]. A generic Bézier curve of the n^{th} order is defined by a set of points P_i as:

$$B(t) = \sum_{i=1}^{n} \binom{n}{i} \cdot (1-t)^{n-i} \cdot t^i \cdot P_i \qquad (1)$$

where t is the local parameter of B varying in the range $[0\,1]$ and $\binom{n}{i}$ is the binomial coefficient (i.e. $n!/[i!(n-i)!]$). The points P_i are called control points of the Bézier curve and the polygon formed by connecting these points with straight lines is called control or Bézier polygon. Among the many properties of this curve, the most relevant are:

- the curve starts and ends in the first and last control point, respectively; in general the intermediate control points do not lie on the curve and their position define the "way" the end points are connected;
- the start (end) of the curve is tangent to the first (last) section of the Bézier polygon;
- the convex hull of the Bézier polygon contains the curve.

The last property turns out to be very useful because it allows drawing complex curves that always lie within a predefined area, with a reduced number of parameters. In other words, the last property simplifies the drawing of geometrically feasible slot profiles.

Being the slot profile of a generic double cage structure made of 3 parts (outer and inner slots and connecting slit), each of these parts can be defined with a n^{th} order Bézier curve. The proposed new variant of Boucherot bar (hereafter referred

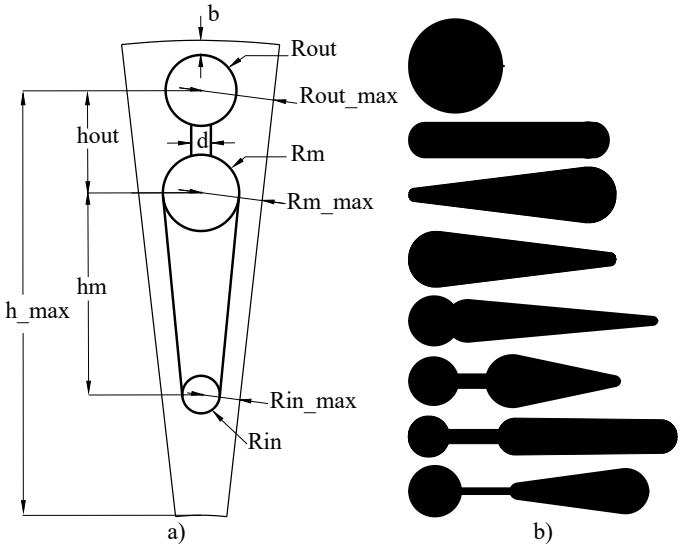

Fig. 2: a) Generalized Boucherot bar parametrization which can generate both single (SC) and double cage structures (DC), b) examples of geometries obtained using this parametrization.

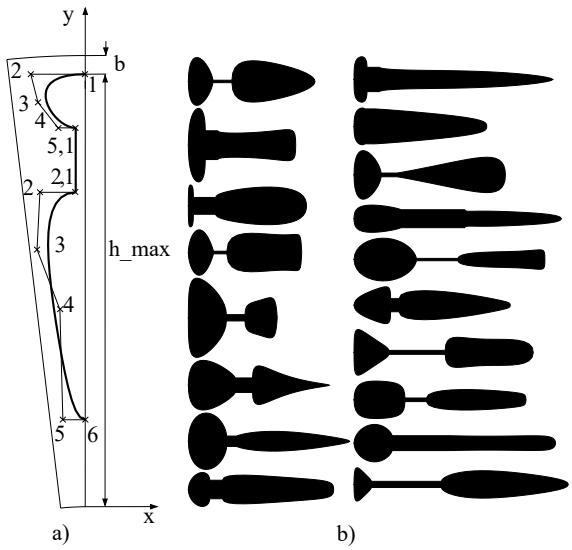

Fig. 3: a) Parametrization of the improved Boucherot bar (IDC), b) examples of geometries obtained using this parametrization.

as improved double cage IDC) is made of a composite Bézier curve, i.e. a series of curves where the last point of one curve coincides with the starting point of the next curve. Fig. 3a) shows an example of this new parametrization drawn considering 5 control points for the outermost slot, 2 for the connecting slit and 6 for the innermost one. If the position of the control points move within the area defined by half of the rotor slot pitch, the resulting slot is always geometrically feasible; the following additional constraints have been considered during the drawing procedure:

- the first and last point of each curve always lies on the middle axis of the slot;
- the radial coordinate of the first two (and last two) control points of each curve are set to be equal in order to have the start (end) of the curve tangent to the initial (last) straight line of the Bézier polygon (and so avoid cuspids at the top and bottom of the bar);
- once the profile of half slot is drawn, the other half is obtained by mirroring (also in this case asymmetric geometries are excluded).

Considering the above constraints, the position of the i^{th} control point is defined by its per unit coordinates $(x_{pu}(i), y_{pu}(i))$ as:

$$\begin{cases} y(i) = y(i-1) \cdot [1 - y_{pu}(i)], & i > 1 \\ x(i) = x_{pu}(i) \cdot x_{max}(y(i)) \end{cases} \tag{2}$$

where $y(1) = h_{max}$ is the maximum available radial space for the slot and $x_{max}(y(i))$ is the tangential limit at the particular radial coordinate $y(i)$ defined by the boundary of the maximum available slot area. Adopting this parametrization, the number of parameters $N(c)$ needed to define the c^{th} Bézier curve of order $n(c)$ is:

$$\begin{cases} N(c) = 2 \cdot n(c) - 5, & if\ n(c) > 2 \\ N(c) = 0, & if\ n(c) = 2 \end{cases} \tag{3}$$

where the last condition holds only when the Bézier curve has to 2 control points, so it becomes a straight line and the latter is set to be parallel to the middle axis (otherwise $N(c) = 1$). Clearly the widening of the slot shape variety, which can be investigated during the design optimization, comes at the cost of an increased number of geometrical parameters to be identified. Considering a slot profile made of three Bézier curves defined by 5, 2 and 6 control points leads to 12 total variables, which is double the number of variables required by the standard Boucherot parametrization (excluding the bridge thickness b).

IV. Performance evaluation

The performance of a three phases SCIM during symmetric operating condition can be estimated, with a good accuracy and a reasonable computational cost, by solving the single-phase equivalent circuit (Fig. 4) featuring lumped parameters derived from time-harmonic (TH) or static FE simulations [23], [24] or analytical formulations [7]. The latter are often used to calculate the 3D parameters ($L_{ew}, L_{ring}, R_{ring}$), while the FEAs allow evaluating the non-linear behaviour of the

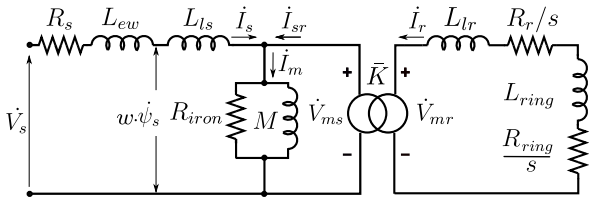

Fig. 4: Equivalent circuit.

remaining 2D parameters (M, L_{ls}, L_{lr}, R_r) . In particular, FE-replicating the indirect experimental tests, i.e. no-load and locked-rotor tests, allows estimating the current dependency of the magnetizing and stator leakage inductance and frequency dependency of the rotor resistance. This approach assumes that the lumped parameters, determined with the FE replicated indirect tests, do not change in the real load scenario. An alternative approach [20], [21] is to carry out a single standstill TH-FE simulation in the load condition of interest. In other words, a non-linear TH-FEAs with a given current and frequency in the rotor reference frame is carried out to determine all the parameters associated with the considered operating point. For each operating condition simulated with a current fed standstill TH-FEA, the magnetizing current $\dot{I}_m$ can be calculated as:

$$\dot{I}_m = \dot{I}_{sr} + \dot{I}_s = \dot{I}_r/\bar{K} + \dot{I}_s \tag{4}$$

where $\dot{I}_s$ is the imposed stator current, $\dot{I}_r$ is the FE calculated current flowing in the reference rotor bar while $\bar{K}$ is the equivalent complex transformer ratio. The stator leakage L_{ls} and magnetizing M inductance follows as:

$$L_{ls} = \frac{|\dot{\psi}_s|}{|\dot{I}_s|} \frac{sin(\angle \dot{I}_m - \angle \dot{\psi}_s)}{sin(\angle \dot{I}_m - \angle \dot{I}_s)},\ M = \frac{|\dot{\psi}_s|}{|\dot{I}_m|} \frac{sin(\angle \dot{\psi}_s - \angle \dot{I}_s)}{sin(\angle \dot{I}_m - \angle \dot{I}_s)} \tag{5}$$

where $\dot{\psi}_s$ is the FE-calculated stator flux phasor, while the equivalent iron loss resistance is:

$$R_{iron} = \frac{3V_{ms}^2}{P_{fe}} \tag{6}$$

where P_{fe} are the stator FE iron losses multiplied by $1/s$. Knowing the voltage induced on the reference rotor bar $\dot{V}_{mr} = \dot{V}_{ms}/\bar{K}^*$, the rotor parameters can be finally calculated as:

$$R_r = \mathscr{R}_e\left\{ -\frac{\dot{V_{mr}}}{\dot{I}_r} \right\},\ L_{rl} = \mathscr{I}_m\left\{ -\frac{\dot{V_{mr}}}{w\dot{I}_r} \right\} \tag{7}$$

Once all the lumped parameters have been determined, the steady state performance of the SCIM can be estimated solving the equivalent circuit for any desired slip. If the rated operating point, defined as the condition in which the motor provides the rated torque T_{rated}, has to be evaluated, it is necessary to identify the rated slip s_{rated} which is not a-priori known as it strongly depends on the rotor slot geometry. In addition, when the latter is known, several TH-FE simulations are needed to characterize the parameters dependency from the current. With the aim of reducing the computational burden, the iterative procedure, summarized in Fig. 5, has been implemented. For the first two iterations ($i = 1, 2$), the TH-FEA is carried out using guessed values of the rated slip and stator current $s_0(i), I_{s0}(i)$.

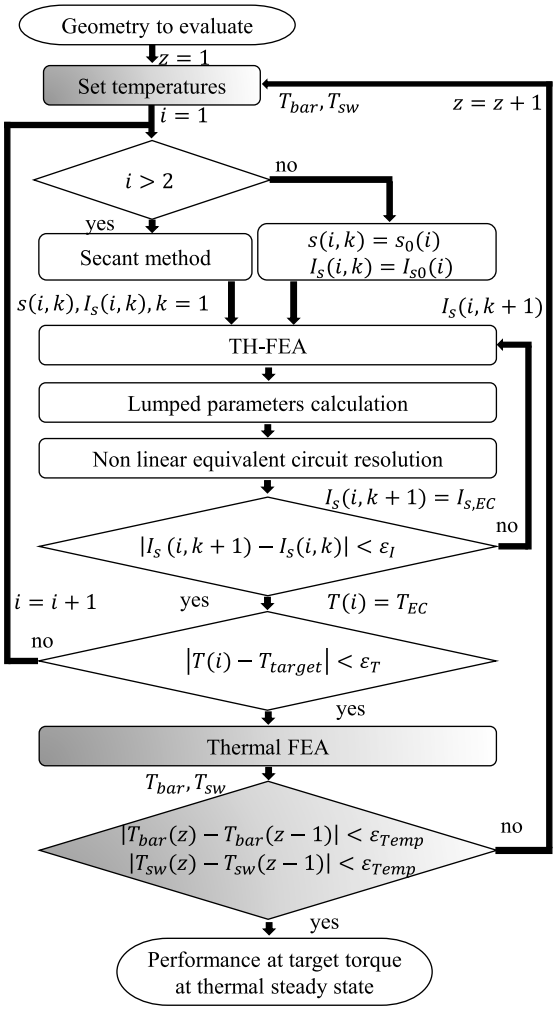

Fig. 5: Flow chart of the iterative procedure aimed at evaluating the machine performance for a given torque.

With the results of the FEA, the lumped parameters of the equivalent circuit can be calculated with the equations (4)-(7) and the non-linear equivalent circuit can be solved. If the FE simulated stator current differs from the one obtained with the equivalent circuit, another TH-FEA is done with the new value of the current, otherwise the current for the given slip $s(i)$ has been correctly identified. If the torque associated with this slip equals the target one (i.e. the rated), the full performance of the target operating point are known, otherwise a new slip is simulated. If the desired torque is not identified in the first two iterations, the slip and stator current to simulate are calculated according to the secant method being fully known the performance at two operating points. The thresholds ϵ_I and ϵ_T, defining the convergence of the current and torque loop respectively, can be identified with a sensitivity analysis trying to balance the accuracy of the performance estimation and the computational cost. The full details of this iterative procedure are reported in [19] along with a methodology to improve the accuracy of the initial guessed values of the rated slip and current (s_0, I_{s0}).

The flowchart in Fig. 5 also reports an external loop (whose blocks are shaded) aimed at identifying the steady state temperatures of stator winding and rotor bar of the geometry under evaluation via a thermal FEA. This loop is not used during the design optimization, i.e. the stator and rotor windings temperatures are set to be constant (T_{sw0}, T_{bar0}).

TABLE I: Baseline machine specifications and parameters

Parameter	Value	Unit
Rated power	11.5	kW
Rated torque	75	Nm
Rated frequency	50	Hz
Rated voltage	400	V_{rms}
Number of poles	4	n.d.
Stator outer diameter	256	mm
Stator inner diameter	165	mm
Stack length	165	mm
Airgap thickness	0.55	mm
Number of stator slots	36	n.d.
Number of rotor bars	28	n.d.

V. Experimental verification

The results of the proposed performance estimation approach are hereafter compared with the experimental results of an off-the-shelf low voltage SCIM whose main dimensions are reported in Table I. This motor is the initial and benchmark design used throughout this work.

The experimental test rig set-up, reported in Fig. 6, consists in the SCIM under test connected to a DC motor via a torque sensor. The armature circuit of the DC motor is connected to a load resistance and the field circuit to a DC power supply allowing to use the DC motor in generating mode regulating the load torque via the field current. Once the thermal steady state condition is reached, the input and output powers have been measured with the torque sensor and the power analyser.

Fig. 7 reports a comparison between the estimated and the measured torque, current and efficiency in per unit as function of the slip in the stable region of the mechanical characteristic. A good agreement is evident in terms of torque and stator current, thus confirming the accuracy of the adopted method. However, the proposed method of analysis always overestimates the efficiency (circa 3% at the rated slip). This is mainly due to the type of FEA performed to estimate the SCIM perfomance (i.e. equivalent circuit parameters). Indeed, non-linear time harmonic FEAs are able to predict the machine behaviour when excited with a single harmonic (in

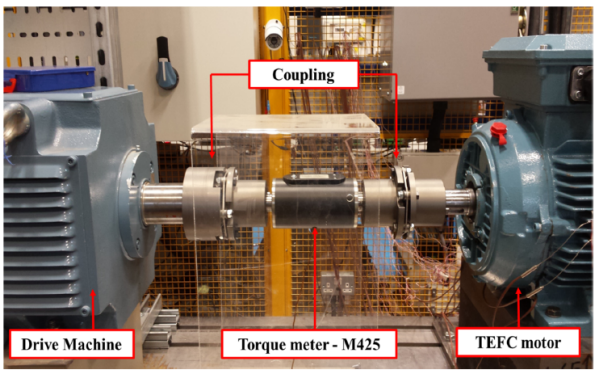

Fig. 6: Test rig set-up.

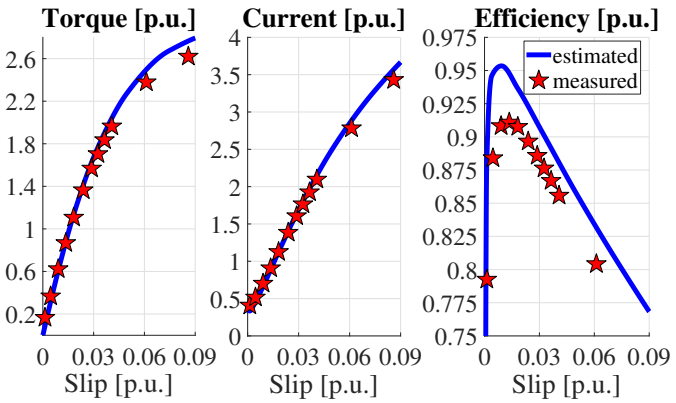

Fig. 7: Estimated and measured torque, stator current and efficiency as function of the slip. Torque and current are expressed in per unit of their respective rated values.

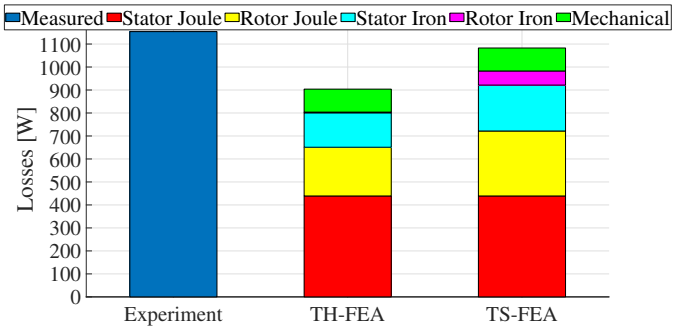

Fig. 8: Comparison of the losses measured and calculated with TH- and TS-FEAs for the rated operating condition.

this case one stator current time harmonic). As a consequent, the loss components due to the higher harmonic content are not predicted, such as the part of the stator iron losses, part of the bar joule losses and all the rotor iron losses. Indeed, Fig. 8 reports the measured total losses at the rated condition and the predicted ones with the proposed approach which make use of TH-FEAs and with the more accurate and time consuming time-step (TS) FEAs. The latter is in good agreement with the experimentally measured total losses. However, it can be clearly seen that the loss calculated with the TH-FEAs underestimate the stator iron losses and the bar joule losses by circa 25% respect with the TS-FEA. In addition, the proposed method is not able to estimate the rotor iron losses being the latter mainly due to higher time harmonic orders. Although less accurate, the proposed performance estimation methodology is suitable to be embedded within an automatic design procedure given its low computational burden. Indeed, one TS-FEA requires approximately 30 minutes while the proposed circuital approach estimating the equivalent circuit parameters with TH-FEAs takes less than 30 seconds [19]. The influence of the various loss approximation on the optimization results will be discussed in detail in Section VII.

VI. Rotor design

A. Optimization procedure

In this work, the design optimizations of the rotor slot are carried out in order to maximize the rated efficiency η_{rated} and the starting torque T_{start} with a constraint on the maximum starting to rated current ratio $k_I = I_{start}/I_{rated}$, i.e.:

$$\begin{aligned} &max\ (\eta_{rated}, T_{start}) \\ &s.t.\ k_I \leq k_{I,max} \end{aligned} \tag{8}$$

The results described in the following sections have been obtained using a multi-objective stochastic optimization algorithm (NSGA-II embedded in Matlab) with a number of functional evaluations proportional to the number of geometrical variables to identify. In particular, a population size of 40 elements evolving for 40 generations has been set when considering the simplest bar geometry, i.e. the single cage structure (SC). The standard double cage structures (DC) are optimized considering 60 elements over 60 iterations, while the more complex geometry (IDC) is analysed with 120 elements for 120 generations. The stator geometry has been kept constant during the whole optimization process and the main geometrical parameters and specifications of the baseline machine are reported in Table. I. The maximum current ratio has been constrained to $k_{I,max} = 7.5$ while keeping unchanged the rotor slot surface (to the value of the baseline SCIM $A_{slot} = 134\ [mm^2]$).

B. Optimization results

Fig. 9 reports the results in terms of Pareto fronts of three optimizations carried out considering the parametrizations described in Section III. All designs were performed considering the bridge thickness b equal to the minimum imposed by manufacturing consideration (0.5mm). As expected, passing from a single to a double cage rotors leads to a relevant improvement of the starting torque and a minor but not negligible increase of the rated efficiency. The efficiency improvement is almost negligible for designs featuring low starting torques while it steeply increases to 1.2% as T_{start} increases. The starting torque improvement increases as the efficiency decreases and goes from 50 to 110 Nm, i.e. from 30 to 60 %.

Adopting the improved double cage parametrization (IDC) allows achieving better performance in the medium-high starting torque range with respect to the standard Boucherot geometries (DC). Conversely, for low-medium starting torques, these two parametrizations provide the same performance.

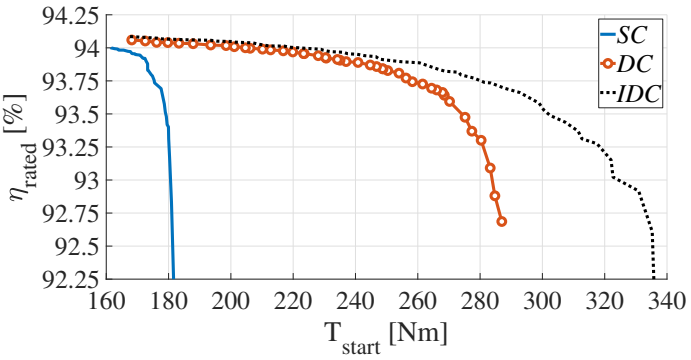

Fig. 9: Pareto fronts obtained with the single cage (SC), the standard Boucherot bar (DC) and the improved one (IDC).

In particular a maximum rated efficiency gain of 1% is accomplished for design delivering a starting torque of 280 Nm while a starting torque gain of 45 Nm is attained comparing machines having the rated efficiency equal to 92.75%. Both improvements strengthens up as the starting torque increases.

It is worth highlighting that the Pareto fronts of double and improved rotor slots tend to converge to the same efficiency as the starting torque decreases. This behaviour is justified by the fact that the parametrizations tends to provide similar optimal geometries in the low starting torque range, as will be discussed in the next section.

VII. Analysis of the Optimal Machines

In the following three subsections, a subset of optimal machines is selected from the Pareto fronts and further analyzed. In particular, subsection A investigates the behaviour of the optimal geometries in terms of the equivalent circuit rotor parameters. Subsection B examines the influence of the temperature on the rated performance, while the last subsection reviews the optimal machine results with more accurate TS-FEAs.

A. Rotor equivalent circuit parameters analysis

A series of machines providing the same starting torques are chosen from the three Pareto fronts and Fig. 10 shows their current density distributions at the starting and rated conditions. Analyzing the latter, the following considerations can be done.

- Considering the single cage optimal geometries, the most efficient solutions are achieved with inverse-trapezoidal bar shapes (i.e. a trapezoid with the major base on the bottom). To obtain an increment of the starting torque, the slot geometry evolves from the inverse-trapezoid via a rectangular-shape to a direct-trapezoid slot. By doing so, the current density distribution becomes slightly higher at the top of the bar and so a small increment of the starting torque is possible. Nonetheless, the single cage structure is able to reach a substantial lower starting torque with respect to the double cage variant being unable to properly exploit the skin effect. This is a well-known clear limitation of the single cage structure when compared to the double cage ones having the same cross-sectional area.
- Both DC and IDC optimizations converge to the same type of geometry, i.e. a double cage connected by a leakage slit. For both optimal geometries, as T_{start} increase, the dimensions of the outer cage increase while the inner one decrease being constant the overall slot area. The total bar length increases with the starting torque and this is mainly ascribed to the connecting slit length increment. On the contrary, the thickness of the latter decreases with T_{start}. Both optimal slot designs feature constant rotor tooth width.
- For both double cage parametrizations, the compromise between starting torque and rated efficiency for a given maximum starting current is due to the difficulty of obtaining a reduction of the starting leakage reactance, needed to satisfy the starting current ratio limit, without increasing the rated leakage reactance. As T_{start} increases the current density distribution is more crowded towards the outer part; this effect increases as more conductive material is exposed to the external periphery of the rotor and as the slit length increases and its thickness decreases. This in turns leads to the twofold desired effects of increasing the effective resistance and decreasing the leakage reactance at the starting condition as shown in Fig. 11a and b. Unfortunately, the reduction of the leakage reactance at the starting is also obtained with the slit length increment, which causes the increment of the same rotor parameter at the rated operating point (Fig. 11c). The latter leads to the reduction of the rated efficiency being the rated resistance almost constant as the slot surface is unchanged (Fig. 11d).
- In the low-medium starting torque range (i.e. 160-240 Nm), the optimal geometries are really similar and indeed they provide the same rated efficiency.
- As the starting torque increases (up to 290 Nm), the IDC slot is able to provide the same starting torque but with

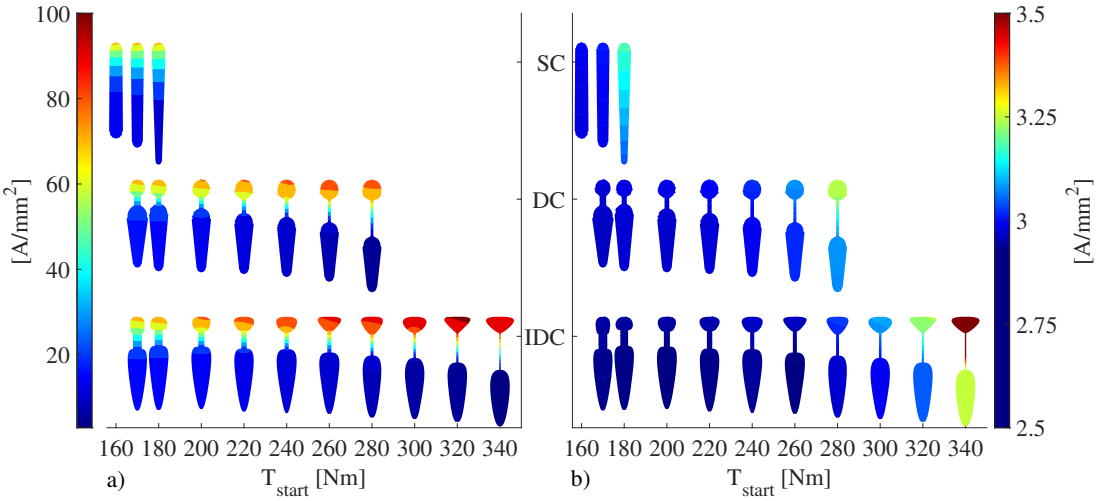

Fig. 10: Current density distributions at the starting a) and rated b) operating conditions of the selected optimal single cage (SC), double (DC) and improved one (IDC).

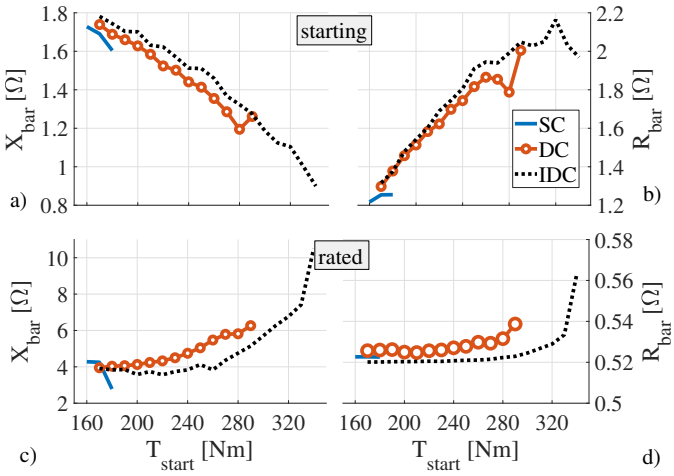

Fig. 11: Rotor equivalent circuit parameters at the starting (a, b) and rated operating conditions (c, d) of the optimal machines.

a better efficiency respect to the DC slot. This is due to both the reduced length of the connecting slit and the better exploitation of the non-uniform current density distribution at the starting condition. In fact, the reduced slit length causes the reduction of the leakage inductance at the rated condition and this in turn leads to a higher rated efficiency. The better exploitation of the non-uniform current density distribution at the starting causes a higher bar resistance with respect to the DC slot, as clearly shown in Fig. 10a. The IDC slot is able to provide the same starting torque thanks to the higher bar resistance at the starting condition as reported in Fig. 11. This effect is due to the fact that the IDC parametrization allows a nail shape outer slot with more conductive material closer to the outer rotor periphery respect with the standard DC slots.

- The above considerations becomes more extreme as T_{start} increases above a certain threshold (290Nm in this case) where only the IDC parametrization is able to provide solutions with starting torques that the DC is not able to produce. It is worth underlining that these extreme slot geometries features very long and thin slit which may be difficult to manufacture and could weaken the rotor mechanical integrity. Nevertheless, analysing the optimal geometries it can be inferred that the general design insights would not change if the upper limit of the slit length and lower limit of its width were constrained during the optimization to a lower and higher value respectively. Indeed, comparing DC and IDC slots having the same starting torque, it can be seen that the slit width is almost equal while the slit length of the IDC is smaller. This is due to the additional degrees of freedom featured by the IDC geometry which leads to the nail-shaped outer cage.
- The higher rated efficiencies given by the IDC slots are also due to the lower rated currents I_s as shown in Fig. 10b). Analysing the latter it is clear that current density distribution is not uniform, also at the rated operating point, for geometries providing high starting torques. This is clearly due to the extreme slot shapes featuring very high leakage slit length.

B. Combined electromagnetic-thermal performance

It has been shown that the rotor bar geometry has an important effect on SCIM performance including the rotor joule losses. The latter is clearly the most important variable affecting the rotor bar temperature. However, for a given value of rotor Joule losses, it is acceptable to assume that two very different bar shapes feature the same temperature rise. Fig. 12a1,b1) report the temperature distributions of the most and least efficient IDC slots at the rated condition having their own input losses, while in Fig. 12a2,b2) the input losses are swapped. Analysing the figures, it can be stated that the bar geometry heavily affects the rotor joule losses, which in turn determines the rotor temperature; however the geometry does not have a direct influence on the rotor temperature. In fact, very different slots when supplied with the same joule losses feature the same temperature rise. The above consideration is the basis that allows considering constant the stator and rotor winding temperature ($T_{sw0} = 80\,°C$, $T_{bar0} = 100\,°C$) during the design optimization. By doing so, the computational effort is greatly reduced.

Fig. 13 report the rated efficiency and the stator and rotor temperatures (T_{sw}, T_{bar}) calculated at thermal steady state with the iterative procedure outlined in Sect. IV. As expected, the rated efficiency decreases respect to the value obtained during the optimization. Considering the double cage structures (DC and IDC), the efficiency difference is higher for solutions providing high starting torques. Regarding the simplest slot geometry (SC), all the re-evaluated solutions features an almost constant efficiency drop. This is clearly due to the higher steady state temperatures of the latter caused by the higher losses. The optimality of the solutions is anyway preserved even though the difference between the rated efficiency calculated at the thermal steady state and the initially supposed temperature is not uniform along the Pareto front. The higher efficiency of the optimal IDC slots clearly leads to a lower temperature of both stator and rotor windings, which is around 10 °C for machine featuring 280 Nm.

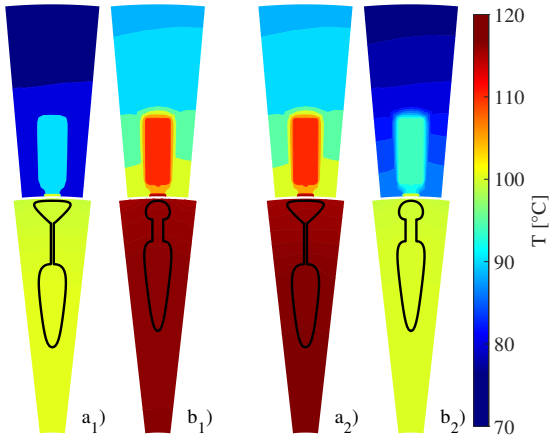

Fig. 12: Temperature distributions of the optimal IDC slots providing 280Nm (a_1) and 180Nm (b_1); temperature distributions of the same slots with the input losses inverted (a_2, b_2).

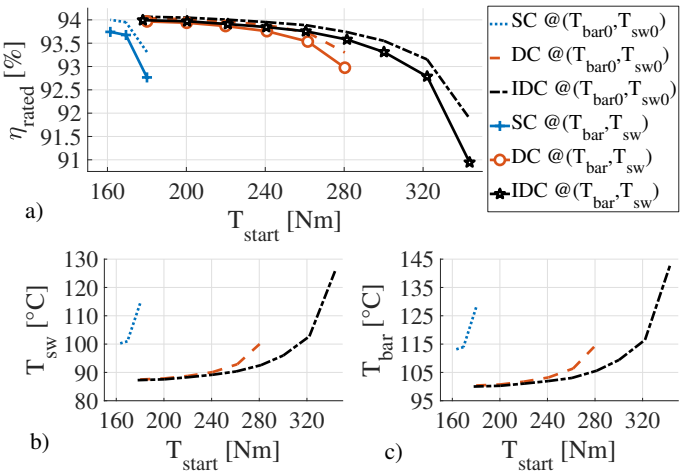

Fig. 13: a) Optimization results re-evaluated at the steady state temperature; b,c) steady state temperature of both stator winding (T_{sw}) and rotor bar (T_{bar}).

C. Time-step FE performance evaluation

Fig. 14a reports the rated efficiency evaluated with voltage-fed time-step (TS) FEAs compared to the one obtained with TH simulations. As expected, the efficiency has been overestimated during the design optimization because the effect of the high order harmonics of the stator and rotor currents were not considered. In fact, the time-harmonic (TH) FE simulations used to derive the equivalent circuit parameters during the design optimization consider only the fundamental stator and rotor currents and only one harmonic in the computation of the iron losses. Including these effects in the performance computation, the rotor joule losses and the iron losses increase, as shown in Fig. 15. The latter reports all the loss components of the optimal machines calculated with TH- and TS-FEAs. Although the stator Joule losses obtained with both types of FEAs are similar, the rotor joule losses and both stator and rotor iron losses present a remarkable difference. Both bar losses and stator iron losses are roughly underestimated by the TH-FEA of about 25% while it is not possible to estimate the rotor iron losses. Both mismatches are clearly due to the losses caused by the higher time harmonic orders of the currents. However, it has to be underlined that the ratios between

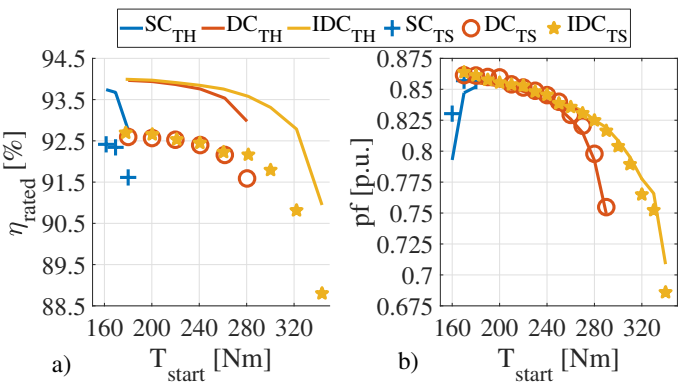

Fig. 14: a) Rated efficiency and b) power factor of the optimal machines evaluated with TH- and TS-FEAs.

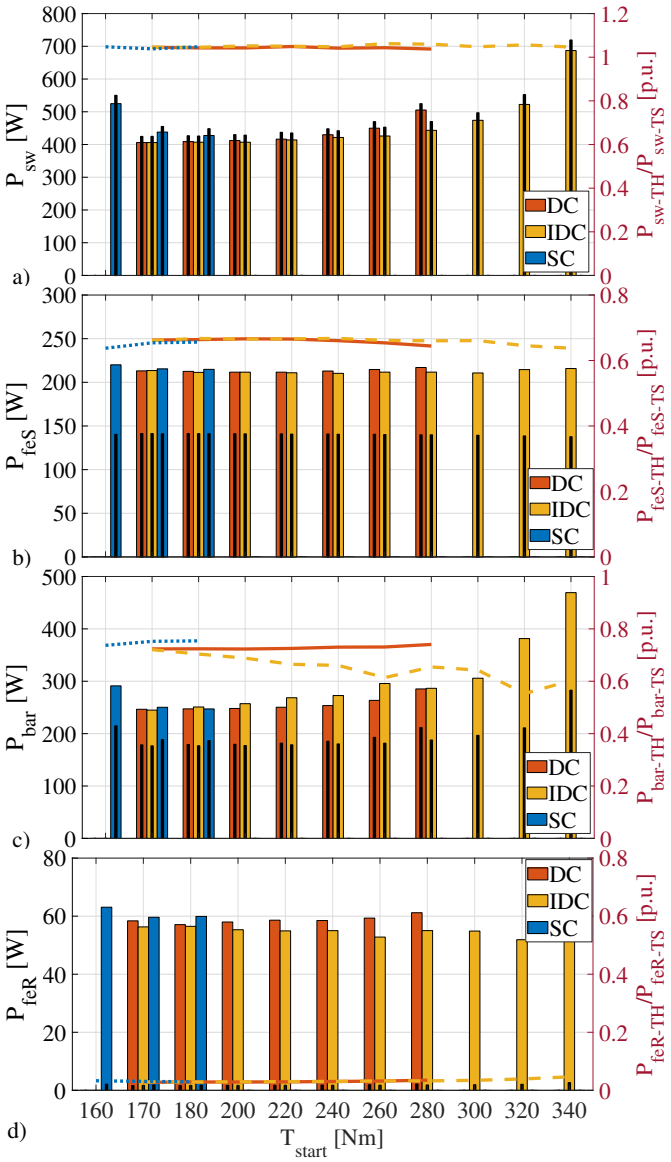

Fig. 15: a) Stator Joule losses, b) stator iron losses, c) rotor bar losses, d) rotor iron losses calculated for the optimal machines with TH-FEAs (black columns) and TS-FEAs (coloured columns). The right axis and the lines show the ratio between the loss components calculated with TH and TS-FEAs.

the losses evaluated with the two methods are approximately constant for all optimal machines as shown on the right axis of Fig. 15. As a consequence, the rated efficiency determined with TS-FEAs is only uniformly shifted towards lower values. It can be concluded that the performance evaluation method, used within the design optimization, provides a reliable estimation of the rated efficiency for a wide range of rotor slot geometries. Indeed, the adopted design procedure guarantees obtaining solutions whose optimality holds even when they are re-evaluated with more accurate time-step FEAs.

Analysing Fig. 15 it can be deduced that along the Pareto fronts the most affected loss components are the stator and rotor Joule losses while the iron losses almost remains unchanged. In addition, the relative weight of the rotor joule losses due to higher harmonics is not constant along the Pareto

front. This effect is more pronounced for the IDC slots as can be seen analysing the ratio between the bar losses calculated with TH- and TS-FEAs (Fig. 15c) which slightly decreases as the starting torque increases. In other words, for certain rotor slot geometries (providing high T_{start}) neglecting the time harmonics effects in the computation of the bar losses becomes relatively more important. Nevertheless, the optimality of the solutions still hold as the bar loss only partially affect the overall efficiency. This minor issue is clearly a pitfall of the adopted method which has to be paid if the design optimization has to be carried out within a reasonable time-frame.
Fig. 14b reports the rated power factor of the optimal machines calculated with both TH- and TS-FEAs showing an excellent agreement. While for the double cage structures the power factor follows the efficiency trends, this does not hold true for the plain rotor slots. This is mainly due to the different behaviour of the rated rotor leakage reactance (Fig. 11c) which decreases as T_{start} increases.

VIII. Conclusion

After a brief historical overview of the most common rotor slot designs, two parametrizations have been selected to be deeply investigated via an automatic design optimization procedure. The implemented performance estimation method allows a really fast prediction of both torque and efficiency although it neglects the influence of the time harmonics on the several loss components. The first selected slot geometry allows exploring the most common single and double cage structures while the second one is a novel variant of the Boucherot slot featuring additional degrees of freedom. Optimizing the starting torque and rated efficiency with a limit on the maximum starting to rated currents ratio, the maximum capability of both rotor slot types are identified. Analysing the obtained results the following final remarks can be drawn.

- Double cage structures definitely outperform the single type ones when maximizing the selected objective function.
- The additional geometrical degrees of freedom of the novel variant of the Boucherot slot allows achieving higher rated efficiency only in the medium-high starting torque range. In the extreme case, it is possible to reach starting torques that the standards slot geometries would not be able to reach.
- This improvement is accomplished with a nail-shaped rotor slot which is able to emphasize the non-uniform current density distribution at the starting condition without excessively lengthen the connecting slit. This leads to a higher starting torque (thanks to the higher starting resistance) and at the same time a better rated efficiency due to the lower rated leakage reactance.
- When re-evaluating the optimal solutions with more accurate time-step FEA also considering the thermal aspect, the optimality of the results is preserved, although for the newly proposed IDC slot geometries the relative weight of the harmonic losses becomes more important.

References

[1] P. Cochran. *Polyphase Induction Motors: Analysis, Design, and Application*. CRC Press, 1989.

[2] S. Williamson and C. I. McClay. Optimization of the geometry of closed rotor slots for cage induction motors. *IEEE Transactions on Industry Applications*, 32(3):560–568, May 1996.

[3] H.A. Toliyat and G.B. Kliman. *Handbook of Electric Motors*. Electrical and computer engineering. CRC Press, 2018.

[4] P.L. Alger. *Induction Machines, Their Behavior and Uses*. Gordon and Breach, 1970.

[5] E. Di Pierro. *Costruzioni elettromeccaniche*. Siderea, 1984.

[6] Zakari Maddi, Abdoune Kadour, and Djamal Aouzellag. Skin effect modelling in induction motors rotor deep bars. 11 2018.

[7] I. Boldea and S.A. Nasar. *The Induction Machines Design Handbook*. Electric power engineering series. CRC Press/Taylor & Francis, 2010.

[8] M. Brojboiu. Concerning the influence of the rotor bar geometry on the induction motor performances. In *5th International Conference on Telecommunications in Modern Satellite, Cable and Broadcasting Service. TELSIKS 2001. Proceedings of Papers (Cat. No.01EX517)*, volume 2, pages 647–650 vol.2, 2001.

[9] O. A. Turcanu, T. Tudorache, and V. Fireteanu. Influence of squirrel-cage bar cross-section geometry on induction motor performances. In *International Symposium on Power Electronics, Electrical Drives, Automation and Motion, 2006. SPEEDAM 2006.*, pages 1438–1443, 2006.

[10] M.G. Say. *Alternating Current Machines*. Wiley, 1983.

[11] M. Di Nardo, A. Marfoli, M. Degano, C. Gerada, and W. Chen. Rotor design optimization of squirrel cageinduction motor - part ii: Results discussion. *IEEE Transactions on Energy Conversion*, pages 1–1, 2020.

[12] A. Boglietti, A. Cavagnino, and M. Lazzari. Computational algorithms for induction motor equivalent circuit parameter determination—part ii: Skin effect and magnetizing characteristics. *IEEE Transactions on Industrial Electronics*, 58(9):3734–3740, Sep. 2011.

[13] A. Boglietti, A. Cavagnino, and M. Lazzari. Modelling of the closed rotor slot effects in the induction motor equivalent circuit. In *2008 18th International Conference on Electrical Machines*, pages 1–4, 2008.

[14] S. Williamson and M. C. Begg. Calculation of the bar resistance and leakage reactance of cage rotors with closed slots. *IEE Proceedings B - Electric Power Applications*, 132(3):125–132, May 1985.

[15] S. Williamson and Y. N. Feng. Slot-harmonic fields in closed-slot machines. *IEEE Transactions on Industry Applications*, 44(4):1165–1171, 2008.

[16] K. Delaere, R. Belmans, and K. Hameyer. Influence of rotor slot wedges on stator currents and stator vibration spectrum of induction machines: a transient finite-element analysis. *IEEE Transactions on Magnetics*, 39(3):1492–1494, 2003.

[17] Mauro Di Nardo, Alessandro Marfoli, Michele Degano, and Chris Gerada. Open and closed rotor slots design of single and double cages induction motor. In *2021 IEEE Workshop on Electrical Machines Design, Control and Diagnosis (WEMDCD)*, pages 125–130, 2021.

[18] T. S. Birch and O. I. Butler. Permeance of closed-slot bridges and its effect on induction-motor-current computation. *Proceedings of the Institution of Electrical Engineers*, 118(1):169–172, 1971.

[19] A. Marfoli, M. Di Nardo, M. Degano, C. Gerada, and W. Chen. Rotor design optimization of squirrel cage induction motor - part i: Problem statement. *IEEE Transactions on Energy Conversion*, pages 1–1, 2020.

[20] D. Genovese, P. Bolognesi, M. De Martin, and F. Luise. A contextual parameter identification method for the equivalent circuit of induction machine. In *2016 XXII International Conference on Electrical Machines (ICEM)*, pages 25–31, Sept 2016.

[21] A. Marfoli, L. Papini, P. Bolognesi, D. Genovese, and C. Gerada. Analysis of induction machine: Comparison of modelling techniques. In *2017 IEEE International Electric Machines and Drives Conference (IEMDC)*, pages 1–7, May 2017.

[22] Marco Paluszny Hartmut Prautzsch, Wolfgang Boehm. *Bézier and B-Spline Techniques*. Mathematics and Visualization. Springer-Verlag Berlin Heidelberg, 1 edition, 2002.

[23] N. Bianchi, S. Bolognani, and G. Comelato. Finite element analysis of three-phase induction motors: comparison of two different approaches. *IEEE Transactions on Energy Conversion*, 14(4):1523–1528, Dec 1999.

[24] L. Alberti, N. Bianchi, and S. Bolognani. A very rapid prediction of im performance combining analytical and finite-element analysis. *IEEE Transactions on Industry Applications*, 44(5):1505–1512, Sep. 2008.

Mauro Di Nardo (M'18) received the M.Sc. (Hons.) degree in electrical engineering from the Polytechnic University of Bari, Italy, in 2012, and the Ph.D. degree in electrical machine design from the University of Nottingham, U.K., in 2017. From 2017 to 2019, he was Head with the AROL R&D Team within the Polytechnic University of Bari leading industrial projects on electrical drives design for mechatronics applications. Since the 2019, he is with the Power Electronics and Machine Control Group of the University of Nottingham as Research Fellow working on wide variety of projects. His research interests include the analysis, modelling, and design optimizations of permanent magnet and synchronous reluctance machines for automotive, aerospace and household sectors, induction motor for industrial applications as well as niche machine topologies such as bearingless and hysteresis motor. He has been serving as an Associate Editor for the Open Journal of Industry Applications since March 2021.

Alessandro Marfoli received the M.Sc. in Electrical Engineering from the University of Pisa, Italy, in 2015 and the Ph.D. degree in electrical machine design from the University of Nottingham (UK) in 2020. He is currently a Research Fellow within the same institution working on wide variety of projects of high industrial and scientific impacts.

His main research interests involves the modelling, analysis and optimization of electrical machines including induction and synchronous machines also for bearingless applications.

Michele Degano (SM'21) received his Master's degree in Electrical Engineering from the University of Trieste, Italy, in 2011, and his Ph.D. degree in Industrial Engineering from the University of Padova, Italy, in 2015. Between 2014 and 2016, he was a postdoctoral researcher at The University of Nottingham, UK, where he joined the Power Electronics, Machines and Control (PEMC) Research Group. In 2016 he was appointed Assistant Professor in Advanced Electrical Machines, at The University of Nottingham, UK. He was promoted Associate Professor in 2020. His main research focuses on electrical machines and drives for industrial, automotive, railway and aerospace applications, ranging from small to large power. He is currently the PEMC Director of Industrial Liaison leading research projects for the development of hybrid electric aerospace platforms and electric transports.

Chris Gerada (SM'12) is an Associate Pro-Vice-Chancellor for Industrial Strategy and Impact and Professor of Electrical Machines. His principal research interest lies in electromagnetic energy conversion in electrical machines and drives, focusing mainly on transport electrification. He has secured over £20M of funding through major industrial, European and UK grants and authored more than 350 referred publications. He received the Ph.D. degree in numerical modelling of electrical machines from The University of Nottingham, Nottingham, U.K., in 2005. He subsequently worked as a Researcher with The University of Nottingham on high-performance electrical drives and on the design and modelling of electromagnetic actuators for aerospace applications. In 2008, he was appointed as a Lecturer in electrical machines; in 2011, as an Associate Professor; and in 2013, as a Professor at The University of Nottingham. He was awarded a Research Chair from the Royal Academy of Engineering in 2013. Prof. Gerada served as an Associate Editor for the IEEE TRANSACTIONS ON INDUSTRY APPLICATIONS and is the past Chair of the IEEE IES Electrical Machines Committee.